scientific reports

OPEN

Targeted imaging of pulmonary fibrosis by a cyclic peptide LyP-1

Jing Li[1,2,3,6], Rui Shu[1,6], Tian Peng[1,6], Zifeng Yang[2], Mingzi Yang[1], Fengjiao Hu[1], Zhangqian Tao[2], Ying Hong[2], Zhiwei Cai[2], Jing Jia[2], Lu Wan[4], Song Tian[1], Zhi-Gang She[1,2], Hongliang Li[1,2,3]✉, Xiao-Jing Zhang[1,3]✉ & Ejuan Zhang[1,5]✉

Pulmonary fibrosis (PF) is an interstitial chronic lung disease characterized by interstitial inflammation and extracellular matrix deposition, resulting in progressive lung dysfunction and ultimate respiratory failure. However, lacking of precise and noninvasive tracers for fibrotic lesions limits timely diagnosis and treatment. Here, we identified LyP-1, a cyclic peptide, as a specific and sensitive tracer for PF detection using PET/CT imaging. FITC-LyP-1 selectively recognized fibrotic regions in bleomycin-induced PF mice, indicating its targeting capability. The colocalization of FITC-LyP-1 with extracellular collagen I within the fibrotic lesions validated its specificity, and further analysis revealed several potential target molecules. In the in vivo application studies, radiolabeled [^{68}Ga]Ga-LyP-1 showed significantly increased lung uptake in PF mice, specifically enriching fibrotic regions on PET/CT imaging. Notably, compared to CT imaging that showed increased mean lung density throughout the phases after bleomycin-administration, lung uptake of [^{68}Ga]Ga-LyP-1 was only increased in the later phase, indicating that LyP-1 recognizes the fibrous changes rather than the inflammatory cells in vivo. These results suggest that the new radiotracer [^{68}Ga]Ga-LyP-1 specifically detects the extracellular matrix in fibrotic lungs. LyP-1 shows promise as a noninvasive tracer for assessing human pulmonary fibrosis, offering potential for improved diagnostic accuracy and timely intervention.

Keywords Pulmonary fibrosis, LyP-1, Positron emission tomography, Tracer, Peptide, Non-invasive imaging

Pulmonary fibrosis (PF) is a frequent interstitial lung disease that leads to progressive lung structural reconstruction, gas-exchange dysfunction, and ultimate respiratory failure or even death[1,2]. It is estimated that PF could be caused by more than 200 separate disorders, such as infection, chronic hypersensitivity and autoimmune connective tissue diseases, or unknown origin. The common histological changes in PF are characterized by chronic interstitial inflammation, proliferation and accumulation of myofibroblasts and fibroblasts, and deposition of extracellular matrix, resulting in decreased lung compliance and oxygen exchange capacity[3,4]. To date, there is a lack of targeted and specific agent and regimen for the diagnosis and therapeutic of PF[5]. Early-stage inflammatory suppression and later-stage fibrogenesis inhibition have not been successful in halting disease progression or reducing mortality[6,7]. Therefore, accurate detection and diagnosis of fibrosis in the lung is highly recommended for the proactively clinical treatment as early as possible to circumvent potential respiratory failure and mortality.

Currently, clinical detection and monitoring of PF is based on the combination of high-resolution computed tomography (HRCT), pulmonary function tests, and peripheral blood biomarkers[8,9]. However, these approaches have limitations in accurately evaluating fibrotic activity and progression, as they are indirect measure of disease outcome[10,11]. Recent studies have highlighted the potential advantages of using radiotracers in positron emission tomography (PET) to target certain functional molecular biomarkers in PF[12,13]. Quinoline-based small-molecule fibroblast activation protein inhibitors (FAPI), originally developed for cancer detection[14,15], are being explored in the context of PF due to the activation of fibroblasts and upregulation of FAP expression observed in its pathogenesis[16,17]. Another tracer, ^{18}F-fluorodeoxyglucose ([^{18}F]FDG), can assess metabolic activity by detecting increased uptake in infiltrated erythrocytes, inflammatory cells and proliferated myofibroblasts in inflammatory and fibrotic lung tissue[18,19]. However, these tracers primarily reflect histological changes that may occur in many

[1]School of Basic Medical Science, Medical Science Research Center, Zhongnan Hospital, Wuhan University, Wuhan, China. [2]Department of Cardiology, Renmin Hospital of Wuhan University, Wuhan, China. [3]State Key Laboratory of New Targets Discovery and Drug Development for Serious Diseases, Gannan Innovation and Translational Medicine Research Institute, Ganzhou, China. [4]Department of Neurosurgery, Huanggang Central Hospital, Huanggang, Hubei, China. [5]Department of Infectious Diseases, Zhongnan Hospital of Wuhan University, Wuhan, China. [6]Jing Li, Rui Shu and Tian Peng contribute equally to this article. ✉email: lihl@whu.edu.cn; zhangxjing@whu.edu.cn; zhangejuan@whu.edu.cn

other lung diseases, such as pneumonia or lung cancer, rather than directly demonstrating the extracellular matrix deposition and fibrous formation, which are key events in tissue fibrogenesis. New sensitive and noninvasive tracers that specifically recognize and discriminate the fibrotic pathological changes including fibrous structures, fibroblast cell activation, and inflammatory responses are urgently required and under investigation[20].

The cyclic peptide LyP-1, consisting of 9 amino acids including Cx7C, was originally identified via phage display for its tumor cell recognition ability[21]. The LyP-1 peptide demonstrates excellent water solubility and stability due to its cyclic structure, formed by a disulfide bond between two cysteine residues[22,23]. Its stability and favorable biodistribution have been well documented in various tumor-targeting studies[24,25]. This peptide recognizes the mitochondrial protein p32, which is known to be overexpressed in tumor cells, tumor-associated macrophages and activated inflammatory cells[26]. LyP-1 recognizes and accumulate in not only tumor tissues and metastatic lesions, but also activated macrophages in atherosclerotic plaques[27,28]. The LyP-1 peptide has a unique ability to penetrate the vessels, pseudocapsules of tumors, and solid fibrous tissues, enable it to reach the diseased lesions and enter the target cells by the CendR motif[29]. Despite the accumulation and activation of inflammatory cells have been observed throughout the progress of lung fibrosis[30], it remains uncertain whether LyP-1 peptide can recognize and bind to fibrotic lung lesions.

In the previous studies, we found that LyP-1 bound with fibroblast-like cells in the atherosclerotic plaques at a low-to-medium level (unpublished data), indicating its potential recognition of fibrous developing areas. Therefore, this study aimed to characterize the recognition and accumulation of LyP-1 in the fibrotic lungs of mice, and to investigate the value of LyP-1-based radioactive tracers for assessing disease progression in bleomycin (BLM)-induced PF mouse models.

Results

LyP-1 recognizes the fibrotic lungs of BLM mice

Intratracheal administration of BLM induces lung injury typically progresses from the initial inflammatory phase (within 14 days) to the fibrosis phase (after 14 days)[31–33]. Consistent with the previous studies, histological analysis of lungs using hematoxylin and eosin (HE) and picrosirius red (PSR) staining revealed focal infiltration of inflammatory cells with minimal fibrosis deposits at earlier stage (day 5). This was followed by progressive fibrosis formation that led to dispersed lesions with thickened interstitial tissue, accumulated inflammatory cells, significant fibrin deposition and focal consolidation of lung at later stage (day 15–18) (Fig. 1a). To assess the fibrosis-targeting capability, LyP-1 and the control peptide ARA were labeled with fluorescein isothiocyanate (FITC) and injected into the mice 18 days after BLM administration. Intravenous injection of FITC-labeled peptides resulted in a strong green fluorescent signal was observed in the lungs of LyP-1-injected BLM mice at 2 h post-injection, while control mice or ARA-injected mice showed weak and nonspecific fluorescent (Fig. 1b). Immunofluorescence analysis using an anti-FITC monoclonal antibody further confirmed the specific binding of FITC-LyP-1 peptides in BLM-induced fibrotic lung tissues, as indicated by the highly overlapping fluorescent signals with FITC autofluorescence (Fig. 1c). The consolidated fibrotic lesion areas exhibited moderate green fluorescence intensity, stronger than the normal alveolar areas, accompanied by some filamentous and intense fluoresce deposition. These results indicate the specific binding capability of LyP-1 to BLM-induced fibrotic lung tissues in mice.

LyP-1 interacts with collagen I-positive components in PF lungs

In order to further investigate the targets recognized by LyP-1 in the fibrotic lung tissue, the localization of the LyP-1 peptide was analyzed by co-staining with cell markers in the lungs of BLM mice. In contrast to previous reports[27], LyP-1 did not co-locate with the majority of CD45 + immune cells (Fig. 2a), F4/80 + macrophages (Fig. 2b), α-SMA^{high} smooth muscle cells (Fig. S1a). Although P32 + cells were found both in the alveolar structure and fibrotic lesions, LyP-1 did not co-localize with P32 + cells (Fig. 2c). Upon co-staining with anti-FITC and phalloidin, it was concluded that LyP-1 was not co-localized with phalloidin, while it appeared to be distributed in the interspaces of phalloidin + cells in the fibrotic area (Fig. 2d). These results suggest that LyP-1 may predominantly bind to the noncellular components in the fibrotic lung tissue.

Positive staining for collagen I was observed in the fibrotic lesions, mainly located in the intercellular spaces away from the cell nuclei[34,35]. The co-localization of LyP-1 peptide with deposited collagen I within these lesions suggests its ability to recognize extracellular matrix components (Fig. 2e). A few LyP-1 peptide was partially localized around α-SMA^{dim} myofibroblasts (Fig. S1b). Moreover, LyP-1 did not directly bind to or penetrate into the primary cells isolated from the BLM-lungs (Fig. S2). These results indicate that LyP-1 may recognize collagen I-positive components in BLM-induced fibrotic lung tissue but not the reported cell types.

LyP-1 recognizes and binds to the extracellular matrix proteins in the fibrotic lungs

To identify potential target proteins of LyP-1 in fibrotic lungs, mass spectrometry analysis was performed using the proteins separated from the homogenate of control- or BLM-lung tissues by affinity chromatography on immobilized LyP-1 or ARA peptides (Fig. 3a,b). The proteins that were increased in LyP-1-BLM sample in comparison to those in LyP-1-control and ARA-BLM samples were identified as unique proteins specifically captured by LyP-1 from the BLM-lungs (fold change > 2, Table S1), with 38 proteins of which were expected to be either secreted or subcellularly located in the extracellular matrix (Fig. 3c). These unique proteins were intersected with the extracellular matrix proteins that were reported increased expression in the mouse lungs after BLM treatment[36,37], and 7 conserved proteins were further focused (Fig. 3d). These proteins, including laminins, myosins, fibrinogen, and biglycan, were the potential targets of LyP-1 in the extracellular interspace of fibrotic lung lesions (Fig. 3e). Mass spectrometry analysis shows that LyP-1 did not capture P32 from the BLM-lung (Fig. 3a), which was consistent with IF analysis in the BLM-lung tissues (Fig. 2c). Therefore, it is evident that LyP-1 specifically targets extracellular matrix proteins rather than P32 protein in the fibrotic lung tissues.

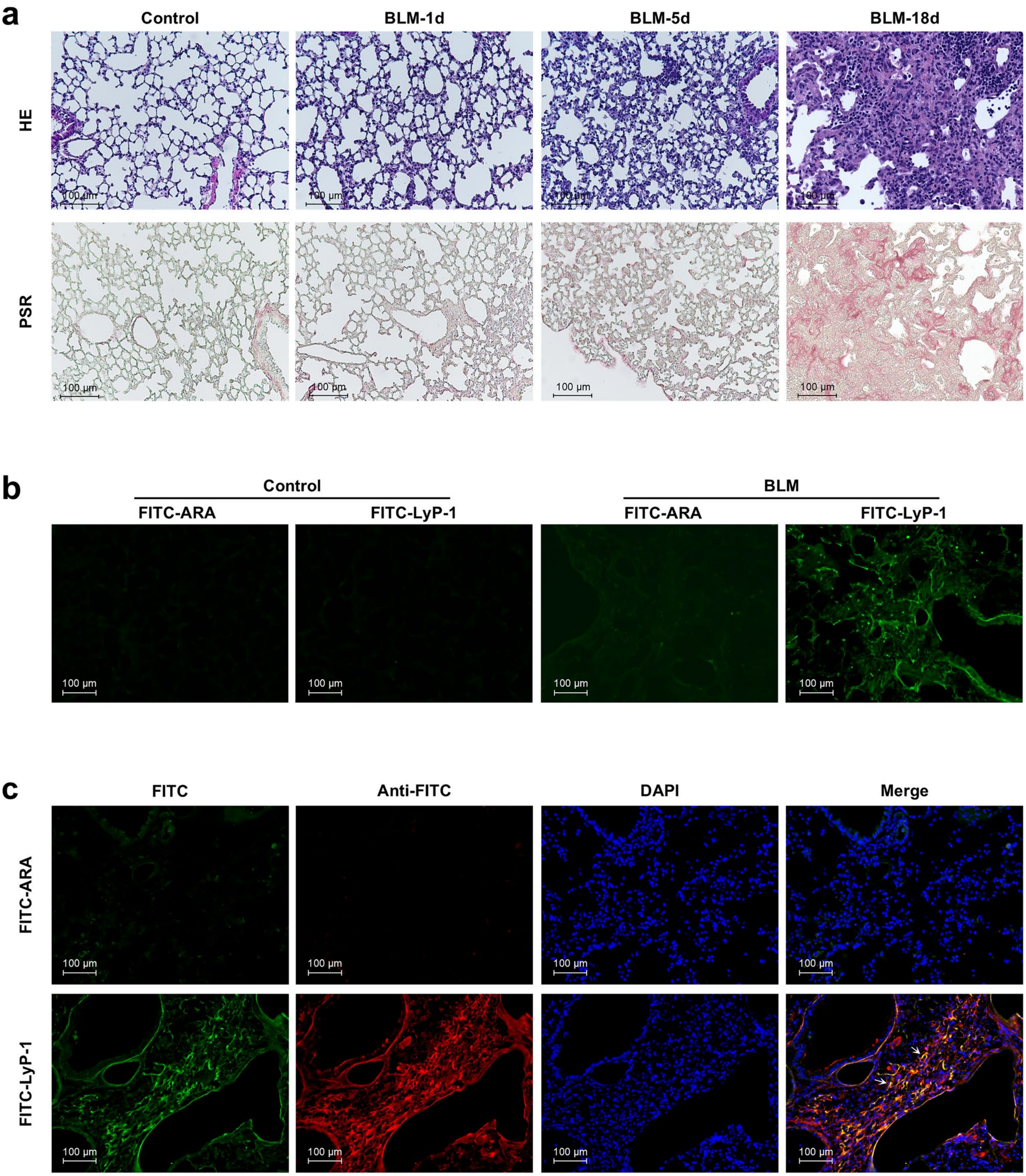

Fig. 1. The LyP-1 peptide binds to fibrotic lung tissue in BLM-injured mice. (**a**) Lung tissues were harvested from the BLM instilled mice at day 1, day 5 and day 18. Representative HE-stained and PSR-stained lung sections at day 1, day 5 and day 18 after BLM instillation. (n = 3 ~ 6 mice per group). (**b**) Mice were i.v. injected with FITC-labeled ARA or LyP-1 peptides at day 18 after BLM instillation. Peptides were allowed to circulate for 2 h, and lungs were harvested after perfusion for frozen sections. Peptides in the lung sections of control or BLM instilled mice were visualized by direct observation of FITC fluorescence (green). (**c**) Peptides in the lung sections of BLM instilled mice were further visualized by immunohistochemical staining with anti-fluorescein antibody (anti-FITC; red) and were counterstained with 4,6-diamidino-2-phenylindole (DAPI; blue). The threshold was equally enhanced for all samples using ImageJ. Representative sections of ARA or LyP-1 peptide binding to lung tissue of control mice or BLM mice are shown (n = 4 ~ 7 mice per group). Scale bar = 100 μm.

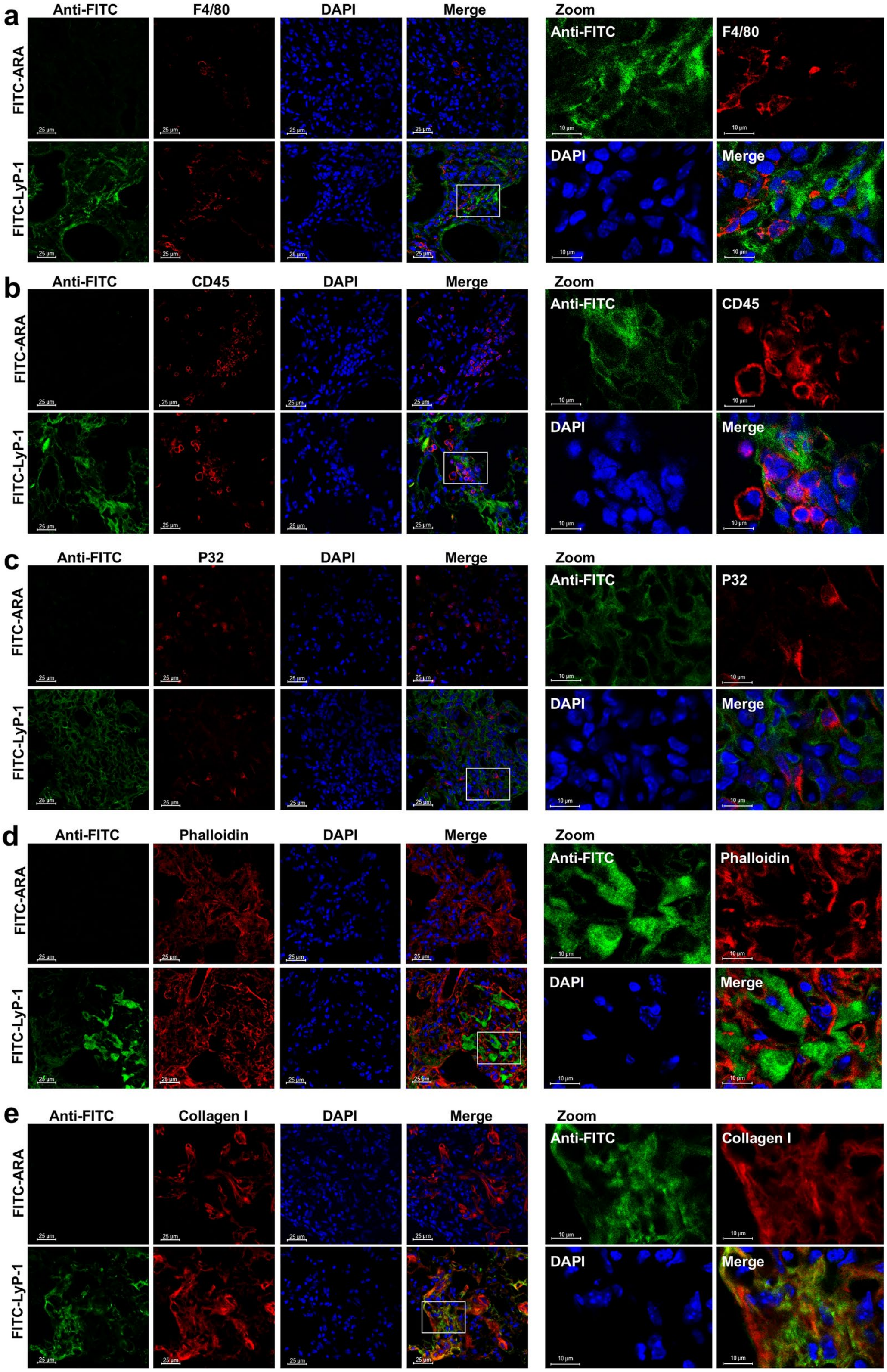

LyP-1 peptide selectively homes to the fibrotic lung in vivo

To further ascertain the distribution and binding of LyP-1 to diseased lung tissue in vivo, fluorescence imaging of organs was carried out. Significantly stronger fluorescence was observed in the lungs of LyP-1-injected BLM mice than in all the other groups at 2 h after FITC-labeled peptide injection, indicating the binding of LyP-1-FITC to the lungs of BLM mice (Fig. 4a). The binding of LyP-1-FITC to control lungs was negligible, which was in concordance with the fluorescence of frozen sections shown in Fig. 1. Weak binding of ARA-FITC to BLM lungs was occasionally observed only in the mediastinal region of some animals. Strong fluorescent signals were observed in the gallbladders and kidneys, suggesting that peptide was metabolized and excreted via the kidney.

◂**Fig. 2**. LyP-1 colocalizes with extracellular components such as collagen I. Mice were intravenously injected with FITC-labeled ARA or LyP-1 peptides at day 18 after BLM instillation. Peptides were allowed to circulate for 2 h, and lungs were harvested for frozen sections. The sections were stained for cell markers (shown in red) including F4/80 (**a**) and CD45 (**b**), anti-P32 (**c**), the cytoskeleton marker phalloidin (**d**), collagen I (**e**), and peptides using anti-fluorescein antibody (anti-FITC; shown in green) and were counterstained with 4,6-diamidino-2-phenylindole (DAPI; shown in blue). Immunofluorescence images showed the localization of FITC-LyP-1 in the fibrotic region of lung sections from BLM mice. The threshold was equally enhanced for all samples using ImageJ. Representative sections of ARA or LyP-1 peptide binding to lung tissue of BLM mice are shown (n = 4 ~ 6 mice per group), with scale bars of 25 μm for the full field view. For magnified (zoom-in) areas, scale bars represent 10 μm.

The binding of LyP-1-FITC and ARA-FITC to other organs was negligible (Fig. 4b). These results indicate that LyP-1 may recognize the fibrotic lungs and home to the diseased lesions in animals.

Design, radiosynthesis and characterization of ^{68}Ga-radiolabeled LyP-1

To determine the distribution and enrichment of LyP-1 in vivo, radiolabeled LyP-1 was designed for PET/CT imaging. To maintain the cyclic structure of the LyP-1 peptide as well as the CendR motif, DOTA was conjugated with the -NH_2 of the cysteine at the N-terminus of LyP-1 either directly or via the 6-aminocaproic acid (ACP) spacer (Fig. 5a). Without the spacer, DOTA-LyP-1 failed to be labeled by $^{68}GaCl_3$ (Fig. 5b). ^{68}Ga-radiolabeled DOTA-ACP-LyP-1 showed a sharp peak of successfully ^{68}Ga-labeled LyP-1 by reverse-phase high-pressure liquid chromatography (RP-HPLC) analysis, while approximately 50% of contaminated free ^{68}Ga was detected. Purification with C18 Sep-Pak resulted in > 99% purity of [^{68}Ga]Ga-DOTA-ACP-LyP-1, which was renamed [^{68}Ga]Ga-LyP-1 for the following experiments (Fig. 5c). The synthesis procedures used consistently yielded approximately 30% (decay corrected) radiochemical pure [^{68}Ga]Ga-LyP-1. ^{68}Ga radiolabeled DOTA-ACP-ARA peptide ([^{68}Ga]Ga-ARA) was used as a control.

In vivo distribution and recognition of [^{68}Ga]Ga- LyP-1 in BLM-treated mice

Mice that received BLM or saline were used to detect the in vivo distribution of [^{68}Ga]Ga-LyP-1 or [^{68}Ga]Ga-ARA at 1 h and 2 h after intravenous injection of radiolabeled peptides. The PET/CT images of [^{68}Ga]Ga-ARA and [^{68}Ga]Ga-LyP-1, along with the standardized uptake value (SUV) quantification of radioactivity content in each organ, revealed low levels of radioactivity in the majority of organs except the kidney and bladder at 1 h and were mildly decreased at 2 h post-injection (Fig. 6a, b), indicating that both of the ARA and LyP-1 peptides are excreted rapidly via urine. Increased uptake of [^{68}Ga]Ga-LyP-1 was observed in the lungs of BLM-treated mice at 1 h post-injection ($p < 0.05$) and significantly decreased at 2 h. Conversely, almost no [^{68}Ga]Ga-ARA was detected in the same group of animals (Fig. 6b). These results suggest that [^{68}Ga]Ga-LyP-1 recognizes and binds to the BLM-induced fibrotic lungs in vivo.

[^{68}Ga]Ga- LyP-1 specifically binds to fibrotic sites in the lung

CT images showed a remarkably increased density in the lung tissue of BLM-treated mice, both at day 5 and day 18 after administration in comparison to the control counterparts (Fig. 7a,b; CT panel). While CT images at day 5 showed a reduction in lung transparency, CT images captured at day 18 displayed scattered, focal, or regional consolidations with increased density in the BLM mice (Fig. 7a,b; CT panel). Quantitative analysis of mean lung density of the CT images demonstrated a significant disparity between control groups and BLM groups at both day 5 and day 18 (Fig. 7c).

Consistent with the histological changes presented in Fig. 1a, increased uptake of [^{18}F]FDG in the lungs was indicative of inflammation at day 5 following BLM instillation. In contrast, [^{68}Ga]Ga-LyP-1 uptake in the lungs at this time point showed no significant differences between BLM and control mice, suggesting that [^{68}Ga]Ga-LyP-1 does not recognize inflammatory lesions (Fig. 7a, PET panel; Fig. 7d). However, [^{68}Ga]Ga-LyP-1 uptake was increased in the lungs of BLM mice at 18 d. Fusion of PET and CT images revealed that the increase in [^{68}Ga]Ga-LyP-1 uptake was mainly concentrated in the high-density areas of CT images, suggesting the specific uptake of [^{68}Ga]Ga-LyP-1 in fibrotic lung areas (Fig. 7b, PET panel). Volumes of interest (VOI) analysis of entire lung tissue in [^{68}Ga]Ga-LyP-1-injected BLM mice showed a significant increase in uptake at 1 h post-injection, compared to that of [^{68}Ga]Ga-LyP-1-injected control mice, [^{68}Ga]Ga-ARA-injected BLM mice and [^{68}Ga]Ga-ARA-injected control mice (Fig. 7e). In addition, the uptake of [^{68}Ga]Ga-LyP-1 was positively correlated with the mean density of the lung measured by CT (Fig. 7f). These results suggest that [^{68}Ga]Ga-LyP-1 binds to fibrotic but not inflammatory lesions in BLM-induced lung diseases.

CT images from control and BLM-receiving mice were analyzed based on the high-density lung areas (− 200 to 300 HU) and normal-density lung areas (− 800 to − 200 HU), which represent the non-aerated lung areas (grey) and aerated lung areas (colored), respectively (Fig. 8a). BLM mice showed a noticeable decrease in the percentage of aerated lung area in comparison to the control mice (Fig. 8b). The uptake of [^{68}Ga]Ga-LyP-1 in the lungs was increased in both the non-aerated lung areas and aerated lung areas, with a slightly higher mean SUV (SUV_{mean}) in the non-aerated lung areas. In contrast, the control group showed similar uptake of [^{68}Ga]Ga-LyP-1 in both non-aerated and aerated lung areas (Fig. 8c). Furthermore, the SUV_{mean} of the [^{68}Ga]Ga-LyP-1 uptake of non-aerated lung areas was also strongly correlated with the mean intensity in the CT images of non-aerated lung areas (Fig. 8d). These results further confirmed the specific binding of [^{68}Ga]Ga-LyP-1 in fibrotic lung areas.

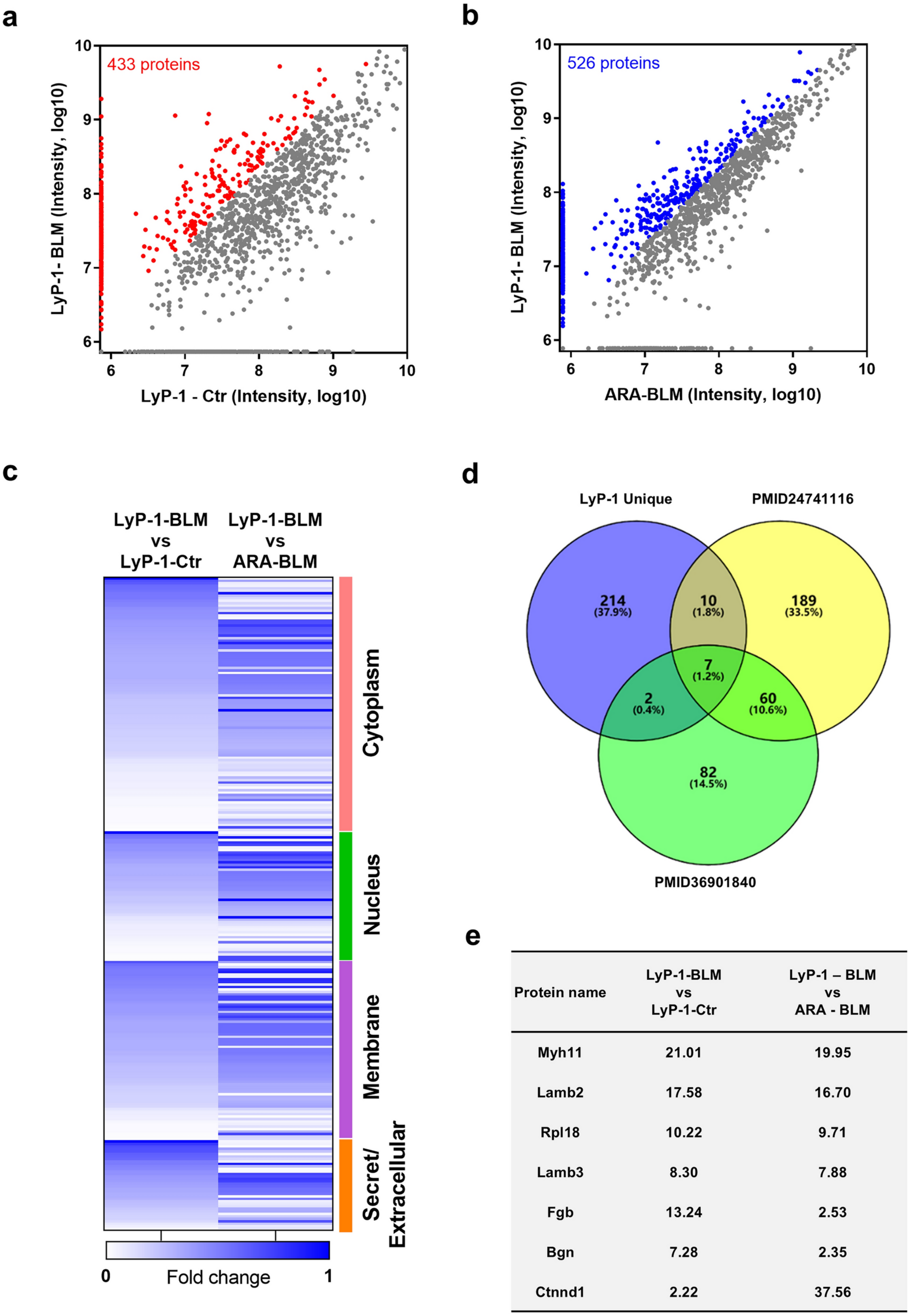

Protein name	LyP-1-BLM vs LyP-1-Ctr	LyP-1 – BLM vs ARA - BLM
Myh11	21.01	19.95
Lamb2	17.58	16.70
Rpl18	10.22	9.71
Lamb3	8.30	7.88
Fgb	13.24	2.53
Bgn	7.28	2.35
Ctnnd1	2.22	37.56

Discussion

Fibrosis is a chronic, progressive, and end-stage pathological change in the interstitial lung diseases that is lack of effective and specific treatment drugs and strategies. Accurate detect and diagnosis of fibrosis is closely related to the clinical therapy and prognosis of PF. Specific tracers for the non-invasive detection of fibrosis are urgently needed to promote early diagnosis, clinical staging, prognostic evaluation and pharmacodynamic monitoring of the disease[38,39]. In this study, we revealed that the cyclic peptide LyP-1 could be used as a new tracer to visualize fibrotic lesions in a BLM-induced PF mouse animal model. The uptake of LyP-1, whether conjugated with fluorescein or the radionuclide, is selectively elevated in fibrotic lung lesions. Furthermore, by in vitro IF

◀**Fig. 3**. Identification of the target protein of LyP-1. Proteins adsorbed by the LyP-1 or ARA peptide loaded affinity chromatography beads were subjected to LC–MS/MS analysis. (**a**) Dot-plots for analysis of protein intensity in the control or BLM-lungs adsorbed by LyP-1 peptide. Upregulated proteins were selected by a fold change > 2 and signed in red dots. (**b**) Dot-plots for analysis of protein intensity in the BLM-lungs adsorbed by LyP-1 or ARA peptide. Upregulated proteins were selected by a fold change > 2 and signed in blue dots. (**c**) Proteins shared by (**a**) and (**b**) were regarded as the unique proteins pooled by LyP-1, and their subcellular location were clustered using UniProt database. (**d**) The LyP-1 unique proteins were intersected with the pulmonary extracellular matrix proteins induced by BLM, and (**e**) the conserved proteins were shown in the list. The reference proteomics resource was shown by the PMID of the original article.

staining of LyP-1 in fibrotic lung sections and in vivo PET/CT imaging, we demonstrated that LyP-1 recognizes fibrosis by binding to collagen-deposited areas but not infiltrated inflammatory cells. Our findings indicate the role of [^{68}Ga]Ga-LyP-1 as a potential noninvasive tracer for the early detection of lung fibrosis.

Lung injury and inflammation are regarded as the key initiators in the pathogenesis of PF, leading to the subsequent activation of a variety of cells, including but not limited to epithelial cells[40], macrophages[41], fibroblasts, myofibroblasts and fibrocytes[42]. Activation and accumulation of intrapulmonary inflammatory cells, activation of fibroblasts/ myofibroblasts and deposition of extracellular matrix within the lung are considered potential targets for noninvasive tracer development[20,43,44]. LyP-1 is an appealing targeting molecule due to its tissue and cell internalization activity, which provides unique advantages for entering and marking solid lesions[27]. In this study, we further illustrated that LyP-1 could recognize fibrotic lesions in the lung. Comparing the distribution of LyP-1 in control or BLM mice, LyP-1 showed accumulated signals only in the fibrotic lungs after BLM treatment, regardless of whether ex vivo detection of the fluorescence of FITC-conjugated LyP-1 in major organs or in vivo monitoring of the radioactivity distribution of [^{68}Ga]Ga-LyP-1 in living mice was used. The increase in the LyP-1 signal is correlated with the progress and severity of tissue damage. BLM-induced pathological changes in the lungs could be characterized as inflammatory infiltration and alveolar destruction at an early stage (in 7 days) and focal fibrosis formation along with decreased inflammation at a later stage (after 7 days)[33]. At the early stage, [^{68}Ga]Ga-LyP-1 accumulation was not detected in the BLM-treated lungs, while it was significantly increased at later stages. This result indicates that LyP-1 tends to bind to fibrotic lesions rather than inflammatory infiltration within the lung.

To date, several PET/CT tracers are under laboratory development, preclinical experiments, or clinical trials. For example, [^{18}F]FDG has shown increased uptake in PET/CT imaging using a BLM-induced lung pulmonary fibrosis mouse model and may provide information on disease severity, prognosis and postoperative acute exacerbation in idiopathic PF patients[45–47]. FAPI-based PET shows elevated radioactivity in BLM-induced and other lung disease mouse models as well[48–50]. However, recognition of the deposited fibrin, collagen matrix and fibrous deposition areas that lack FDG- or FAP-positive cells remains to be investigated. LyP-1 demonstrated specific recognition of fibrotic lung regions, as confirmed by colocalization with collagen I in lung sections and consistent findings from tissue fluorescent imaging and [^{68}Ga]Ga-LyP-1 PET/CT imaging in PF mice. Importantly, we note that the majority of LyP-1 is located extracellularly, indicating that LyP-1 recognizes an extracellular component that is different from that of FAPI, which bind to fibrocytes. In the PET/CT analysis, CT images provide limited information to distinguish inflammation and subsequent fibrosis in the BLM mouse model, while [^{68}Ga]Ga-LyP-1 specifically distinguishes the fibrotic phase of BLM mice. These findings highlight the unique ability of [^{68}Ga]Ga-LyP-1 to specifically detect extracellular matrix deposition in the PF lung tissues, distinguishing it from FAPI and FDG that recognize the cellular components.

P32 protein, as the reported target molecule of LyP-1 expressed on tumor cells and activated F4/80 + macrophages, was predominantly observed in the relatively normal alveolar structure of BLM-mice with a few in the fibrotic structure as well. P32 protein is predominantly located on the mitochondrial and translocated to the cell membrane in specific conditions, where it is recognized by LyP-1 and involved in LyP-1 cleavage and endocytosis. Interestingly, LyP-1 was neither colocalized in these P32 + cells nor F4/80 + cells[27]. Our findings suggest that LyP-1 does not recognize the P32 protein in the lung no matter by IF co-staining or affinity chromatography proteomic analysis. Instead, LyP-1 mainly colocalizes with the extracellular proteins in the fibrotic lung samples. Affinity chromatography using LyP-1 peptide indicated several potential targets that might be recognized by LyP-1 in the extracellular matrix, while the interaction between LyP-1 and these proteins requires further experimental confirmation. Therefore, our study reveals potential novel target molecules of LyP-1 in the fibrotic lung, which are worthy of further molecular biological identification and investigation.

LyP-1 is attractive due to its low immunogenicity, minimal toxicity, and high histocompatibility, all of which have been well documented in both in vitro cytotoxicity tests and in vivo animal studies. LyP-1 has been extensively utilized in various research applications in the forms of metal nanoparticles, semimetallic nanomaterials, and conjugated drugs for PET/CT, CT, MRI imaging and therapeutic purposes in tumors, including several pulmonary tumor cell lines[23,24,28,51–54]. As a result, it is challenging to use LyP-1-tagged tracer for distinguishing lung fibrosis from lung cancer, particularly when lung cancer occurs secondary to pulmonary fibrosis. Therefore, we recommend that LyP-1 can be considered a potential complementary diagnostic agent rather than an independent one. The diagnosis of pulmonary fibrosis or lung cancer should always be based on a comprehensive assessment of clinical symptoms, laboratory tests and characteristic CT imaging[16]. Another advantage of LyP-1-tagged tracers is that it can be used to noninvasively detecting the fibrosis progression. Such detection is beneficial for monitoring the efficiency of clinical treatment. Further studies in our group using [^{68}Ga]Ga-LyP-1 PETCT imaging will focus on exploring its efficacy in distinguishing human lung fibrotic diseases from malignancies, as well as enhancing its diagnostic accuracy and clinical applicability.

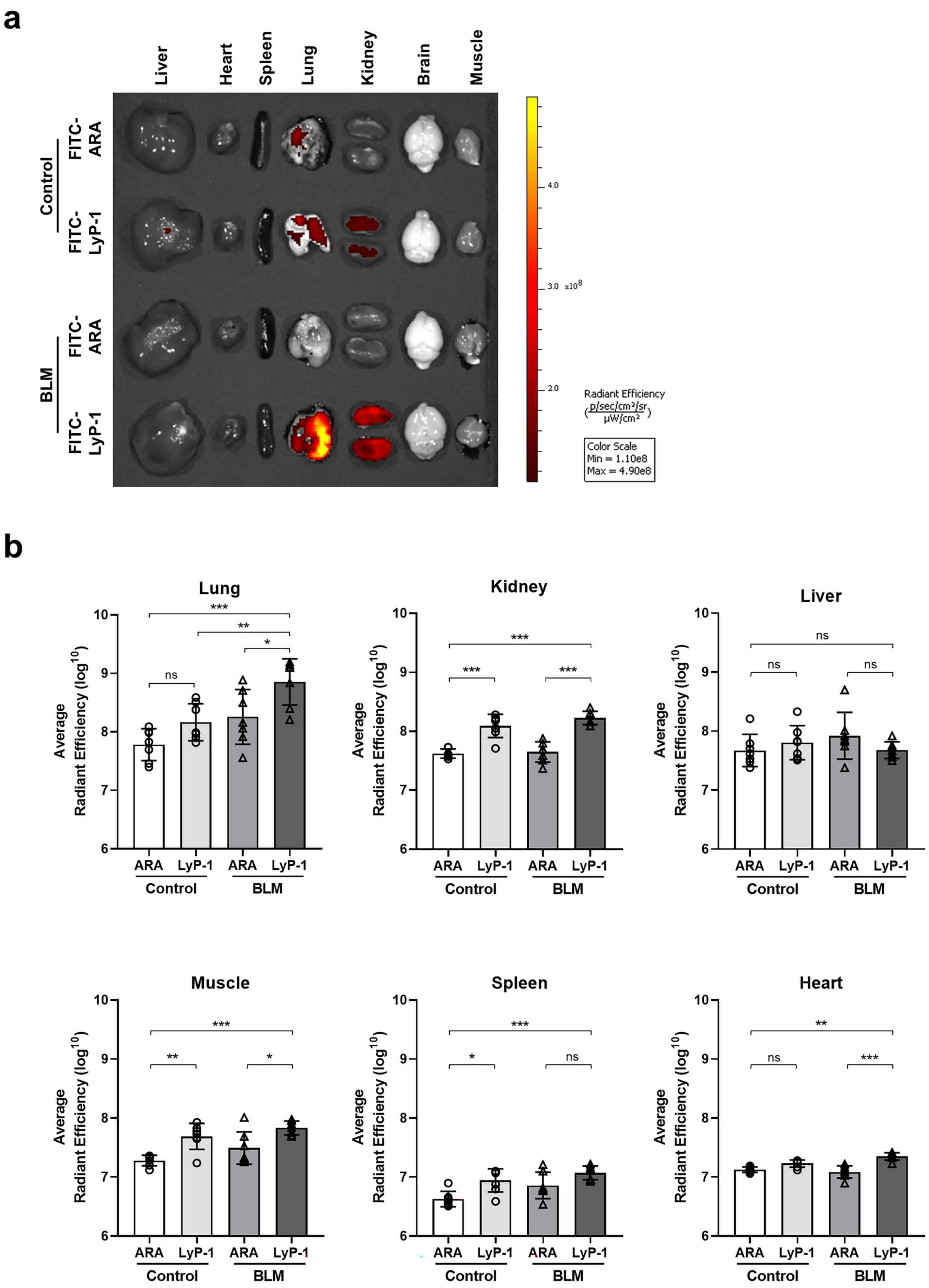

Fig. 4. LyP-1 selectively accumulates in the fibrotic lung in vivo. Mice were i.v. injected with FITC-labeled ARA or LyP-1 peptides at day 18 after BLM instillation, and major mouse organs were collected at 2 h after peptide injection. (**a**) Representative fluorescent images of major mouse organs in each group were obtained by a Li-COR Odyssey infrared imaging system. (**b**) The average fluorescence intensity of FITC in each organ of ARA- or LyP-1-injected control or BLM mice was analyzed. The results are presented as the mean ± SD, n = 7 mice per group. Statistical relevance was determined for each organ by Mann–Whitney test (for lungs), or one-way ANOVA followed by the Bonferroni posttest (for other organs).

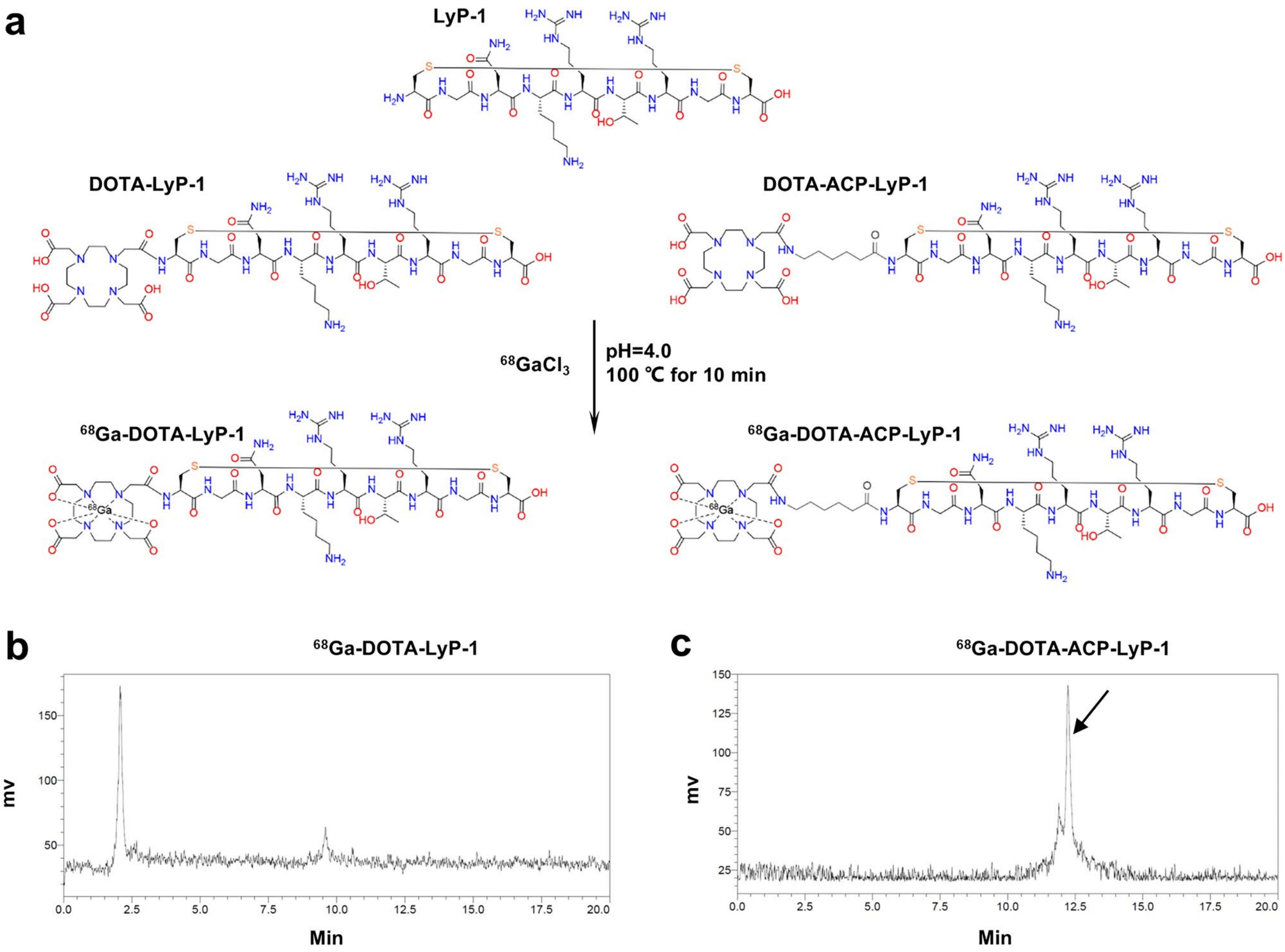

Fig. 5. Design, radiolabeling and radiochemical purity of [^{68}Ga]Ga-LyP-1. DOTA was conjugated to LyP-1 directly or indirectly via an aminocaproic acid (ACP) linker. DOTA conjugated peptides were radiolabeled with $^{68}GaCl_3$ at 100 °C for 10 min at pH 4.0 and purified by C18 Sep-Pak. (**a**) [^{68}Ga]Ga-LyP-1 structure and labeling conditions. (**b**) RP-HPLC chromatograms of purified [^{68}Ga]Ga-DOTA-LyP-1 or (**c**) [^{68}Ga]Ga-DOTA-ACP-LyP-1.

Similar to previous in vivo distribution studies of LyP-1, [^{68}Ga]Ga-LyP-1 is enriched in the liver and heart at a high radioactivity level regardless of BLM treatment[55]. However, histofluorescence imaging that was performed after perfusion of free blood showed low levels of hepatic and cardiac fluorescence intensity, suggesting that the accumulation of LyP-1 in the liver and heart is blood perfusion dependent but not disease specific. These high levels of radioactivity in the liver or heart may cause quantitative error due to spillover effects and partial volume effects[56]. As a result, although [^{68}Ga]Ga-LyP-1 uptake was mainly observed in the non-aerated lung areas, no significant differences in [^{68}Ga]Ga-LyP-1 uptake were found between non-aerated and aerated lung areas due to the increased SUV that was affected by the radioactivity from the liver. In addition, the hepatic artifacts produced by respiratory motion may also affect the measurement of SUV in the lower lobes of both lungs, whereas pulmonary fibrosis predominantly occurs in these regions[57]. Factitious control of respiratory rate or respiratory gated sampling may mitigate the effect of liver artifacts on pulmonary signals. Compared to traditional CT, PET-CT using LyP-1-tagged tracer could show the biological properties of tissue pathology by specifically targeting to fibrosis lesions, overcoming the limitations of CT that was based on the anatomical changes. Meanwhile, specific targeting of LyP-1 to fibrosis allow it to distinguish fibrosis from inflammation, and thus, LyP-1 may reduce the misdiagnosis caused by lung inflammation. Taken together, our results demonstrate that [^{68}Ga]Ga-LyP-1 detects the presence of fibrotic lesions in a pulmonary fibrosis mouse model by annotating the extracellular fibrous matrix, making it a potential noninvasive candidate tracer for the clinical assessment of human pulmonary fibrosis. These findings warrant further investigation to validate its efficiency across different patient populations and disease stages, as well as to address challenges related to targeting specificity, binding affinity, and pharmacokinetics.

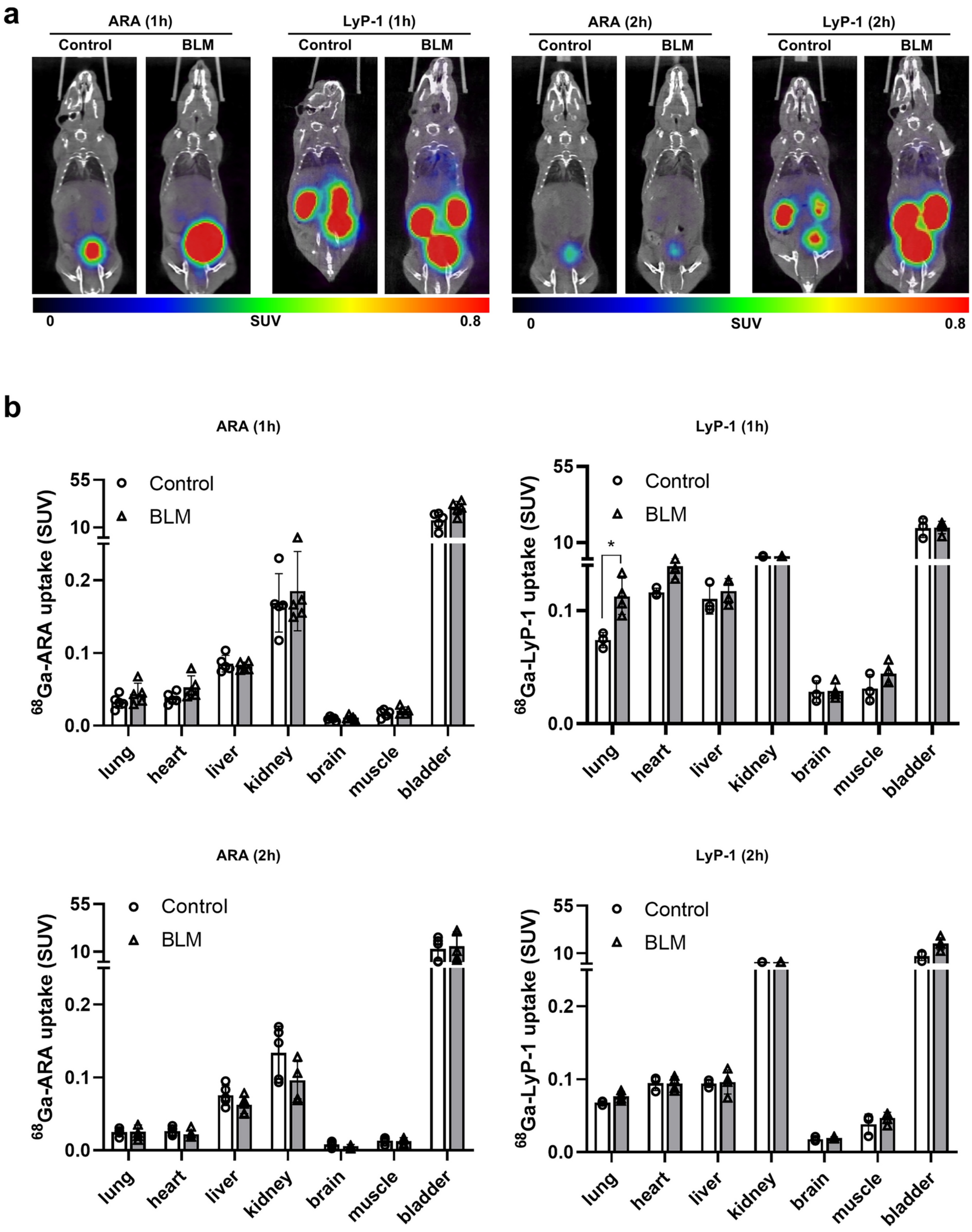

Fig. 6. PET/CT imaging with [^{68}Ga]Ga-LyP-1 shows specific enrichment in the fibrotic lung of BLM mice. Mice were intravenously injected via the tail vein with 5.55–7.4 MBq of [^{68}Ga]Ga-LyP-1 or [^{68}Ga]Ga-ARA. PET/CT scans were acquired at 1 h and 2 h post-injection. (**a**) Representative whole-body PET/CT images with [^{68}Ga]Ga-LyP-1 or [^{68}Ga]Ga-ARA of control and BLM-receiving mice at day18 after BLM instillation. Graph represents the [^{68}Ga]Ga-LyP-1 or [^{68}Ga]Ga-ARA uptake in SUV of control and BLM-receiving mice. (**b**) The VOI of major mouse organs in (**a**) was gated, and the uptake of [^{68}Ga]Ga-LyP-1 or [^{68}Ga]Ga-ARA by each organ at 1 h and 2 h post-injection was analyzed. The results are presented as the mean ± SD (n = 3–5 mice per group). *$p < 0.05$, statistical relevance between the control-lung and BLM-lung tissues was determined by unpaired t test.

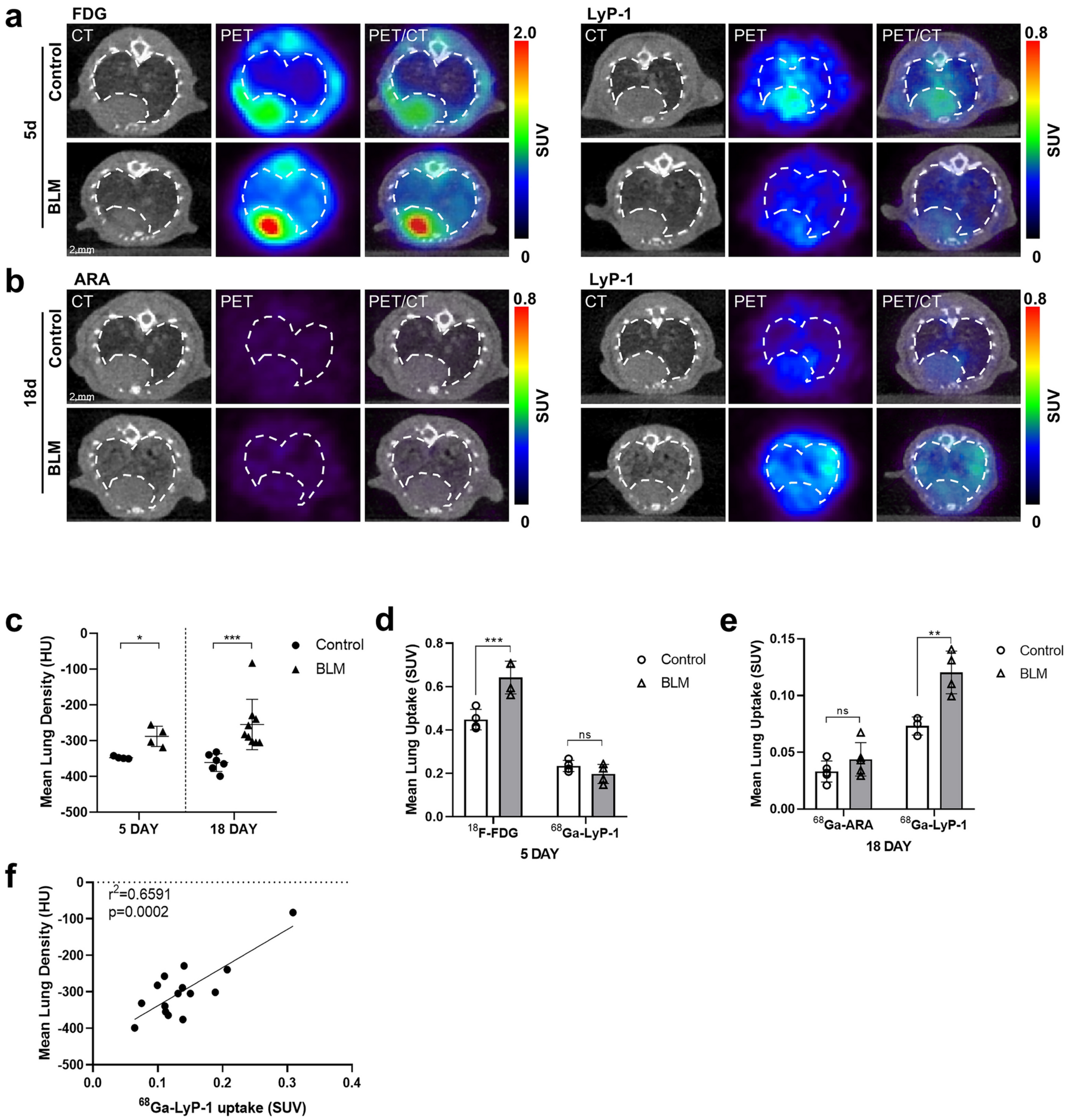

Fig. 7. PET/CT imaging with [^{68}Ga]Ga-LyP-1 specifically distinguishes the fibrotic phase of BLM mice. Mice were intravenously injected via the tail vein with 5.55–7.4 MBq of [^{18}F]FDG, [^{68}Ga]Ga-LyP-1 or [^{68}Ga]Ga-ARA. PET/CT scans were acquired at 1 h post-injection. (**a**) Representative lung PET/CT images with [^{18}F]FDG or [^{68}Ga]Ga-LyP-1 of control and BLM-receiving mice at day 5 after BLM instillation. Graph represents the [^{18}F]FDG or [^{68}Ga]Ga-LyP-1 lung uptake in SUV of control and BLM-receiving mice. (**b**) Representative lung PET/CT images with [^{68}Ga]Ga-LyP-1 or [^{68}Ga]Ga-ARA of control and BLM-receiving mice at day18 after BLM instillation. Graph represents the [^{68}Ga]Ga-LyP-1 or [^{68}Ga]Ga-ARA lung uptake in SUV of control and BLM-receiving mice. (**c**) Graph represents the mean lung density quantified on CT images of (**a**) and (**b**). (**d**) Graph represents the [^{18}F]FDG or [^{68}Ga]Ga-LyP-1 lung uptake in SUV of control and BLM-receiving mice at day 5, and (**e**) graph represents the [^{68}Ga]Ga-LyP-1 or [^{68}Ga]Ga-ARA lung uptake in SUV of control and BLM-receiving mice at day 18. All results are presented as mean ± SD, n = 4 mice per group (**a**, **d**) or n = 5 mice per group (**b**, **e**). $^*p < 0.05$, $^{**}\ p < 0.01$, $^{***}p < 0.001$; statistical relevance was determined by Mann–Whitney test (**c**) or Two-way ANOVA (**d**, **e**). (**f**) The correlation was analyzed between the mean lung density (HU) measured on CT images and [^{68}Ga]Ga-LyP-1 uptake of corresponding lungs at day 18.

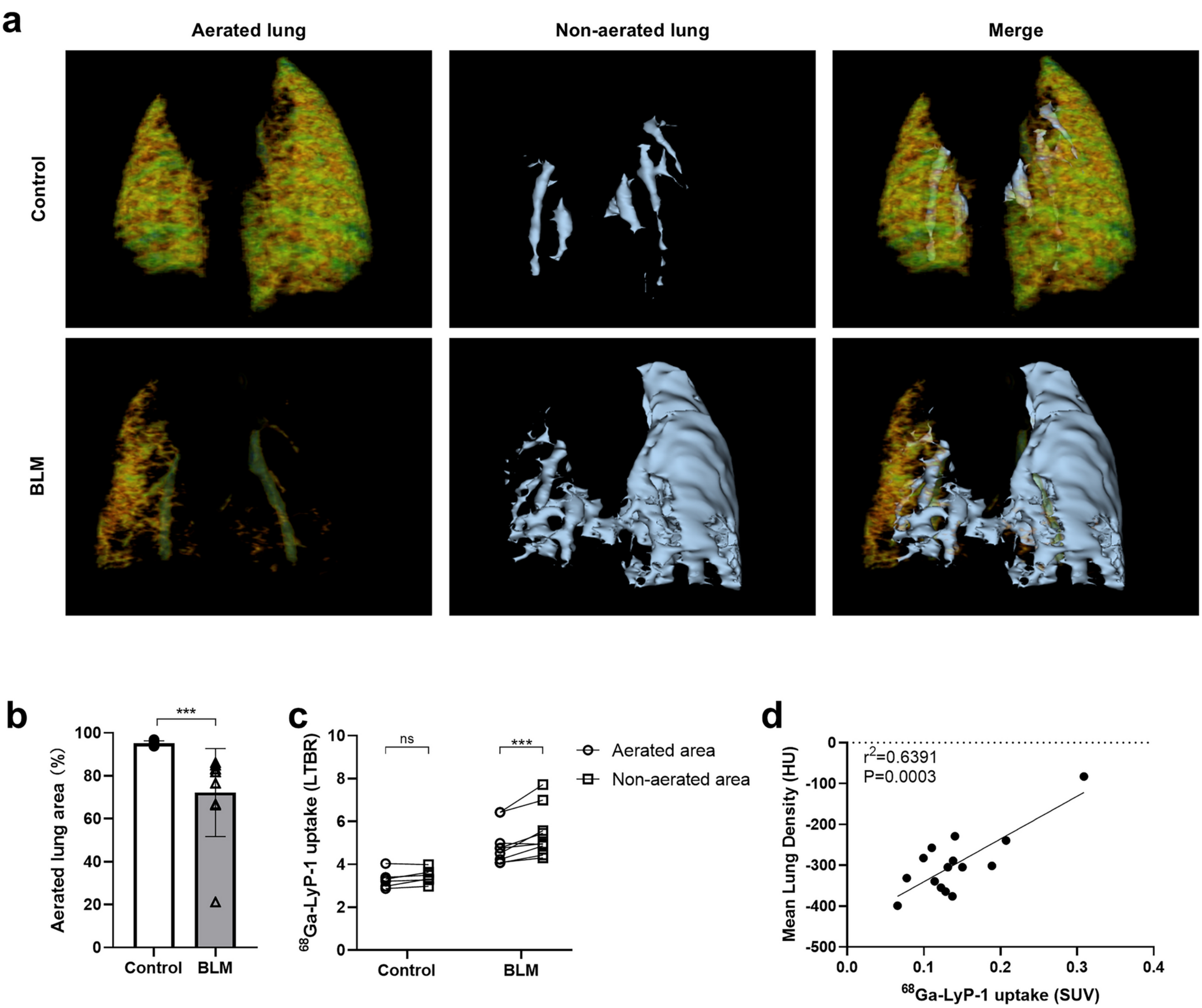

Fig. 8. [^{68}Ga]Ga-LyP-1 specifically binds to the fibrotic sites in the lung. (**a**) Representative 3D reconstruction of lung VOI segmentation of control and BLM-treated mice at day 18. Color represents normal-density lung areas (– 800 to – 200 HU) representative of aerated lungs; grey represents high-density lung areas (– 200 to 300 HU) representative of non-aerated lungs. (**b**) Graph represents the percentage of aerated lung on CT images. (**c**) Graph represents the [^{68}Ga]Ga-LyP-1 lung uptake in SUV of control and BLM-receiving mice at day 18 in aerated and non-aerated lung areas (segmented on CT images). All results are presented as the mean ± SD, n = 6 for control group, n = 9 for BLM group. *$p < 0.05$, **$p < 0.01$, ***$p < 0.001$; statistical relevance was determined by Mann–Whitney test (**b**) or Two-way ANOVA (**c**). (**d**) The correlation between the mean [^{68}Ga]Ga-LyP-1 uptake by the VOI analysis of non-aerated lung areas and the mean lung intensity in the corresponding ROI of CT images at day 18.

Materials and methods

Ethics statements

C57BL/6J male mice at 6–8 weeks of age were purchased from Beijing Vital River Laboratory Animal Technology Company (Beijing, China) and were maintained under specific pathogen-free (SPF) conditions in the Center for Animal Experiment of Wuhan University. The animals received humane care according to the Guide for the Care and Use of Laboratory Animals published by the National Academy of Sciences and the National Institutes of Health. All animal experiment programs were performed according to the Regulations for the Administration of Affairs Concerning Experimental Animals in China (1988) and the Guidelines for Animal Care and Use, Wuhan University. Animal experiments were reviewed and approved by the Animal Care and Use Committee of Renmin Hospital of Wuhan University (permission number: 20191112, 20211106A, 20201219A) and the Experimental Animal Welfare and Ethics Committee, Zhongnan Hospital of Wuhan University (permission number: ZN2022192).

BLM-induced pulmonary fibrosis mouse model

The pulmonary fibrosis model and controls were established using 9-week-old male C57BL/6 mice as described previously[33]. Briefly, mice received a single dose of 2.5 mg/kg bleomycin (BLM) dissolved in 0.9% normal saline at a volume of 8 µL/g by intratracheal injection under anesthesia (3% isoflurane) at day 0. After injection, animals were upright for 1–3 min and gently rotated to ensure uniform distribution of BLM in the lungs. Control mice received 0.9% normal saline following the same procedure. Starting from day 16, bleomycin-treated animals exhibited significant weight loss and severe respiratory distress, and the mortality rate gradually increased. To ensure the welfare of the animals, histological and imaging studies were conducted at an earlier phase (day 5) to capture the inflammation and at a later phase (day 18) to assess the most pronounced pulmonary fibrotic lesions. For some animals that were too weak at later phase after BLM administration, experiment was terminated for histological sampling at around day 15–16.

Peptides

All peptides were synthesized, modified, and purchased from Top-Peptide Biotechnology Company (Shanghai, China). For ex vivo and in vitro tracing, the cyclic peptide LyP-1 (CGNKRTRGC) was synthesized and modified with either fluorescent dyes (FITC) or chelating agents (DOTA). A linear peptide ARA (ARALPSQRSR), composed of nine random amino acids, was synthesized and modified in parallel to serve as a non-relevant control for measuring background signals derived from the non-specific binding of peptides to tissues[21]. Briefly, peptide synthesis was carried out using solid-phase peptide synthesis (SPPS) following the Fmoc protection strategy. For the cyclic peptide (LyP-1), disulfide bond formation was conducted through an oxidation reaction under alkaline conditions. FITC or DOTA was then coupled to the -NH2 residue of the N-terminal cysteine of the peptides via the ACP linker. The modified peptides were purified using reverse-phase high-performance liquid chromatography. Peptide identity and purity were confirmed by mass spectrometry (MS) and high-performance liquid chromatography (HPLC). All peptides reached a purity of > 95% and exhibited normal solubility in water.

Affinity chromatography and mass spectrometry analysis

For identifying LyP-1 binding proteins, mouse lungs were collected at day 18 after saline- or BLM-administration. Lung tissues were lysed in PBS containing 200 mM n-octyl-beta-D-glucopyranoside and protease inhibitor cocktail (Roche). The cleared lysate was loaded on to LyP-1 or ARA peptide coated Sulfolink-agarose beads (Pierce, Waltham, MA) and incubated at 4 ℃ for 3–4 h. The columns were washed with wash buffer (75 mM n-octyl-beta-D-glucopyranoside and protease inhibitor cocktail in PBS). The proteins on the beads were dissolved by using SDS-loading buffer, and enriched by SDS-PAGE. Proteins in the polyacrylamide gel were subjected to liquid chromatography-mass spectrometry (LC-MS/MS) analysis at the Shanghai Bioprofile Technology (Shanghai, China). All mass spectra were analyzed with MaxQuant software version 2.0.1.0. The MS/MS spectra were searched against the Mus musculus UniProt protein sequence database ([10090]-55260-20230321.fasta). The subcellular location of the proteins was analyzed using the UniProt protein subcellular location database.

Radiosynthesis and purification of [^{68}Ga]Ga-LyP-1 and [^{68}Ga]Ga-*ARA*

^{68}GaCl$_3$ was eluted with 4 mL of 0.05 M hydrochloric acid from a ^{68}Ge/^{68}Ga generator (Isotope Technologies Garching GmbH, Garching, Germany) at the Department of Nuclear Medicine of Union Hospital, Tongji Medical College, Huazhong University of Science and Technology. DOTA-conjugated peptide (2 mg/mL, 20 µL) was dissolved in 0.9 mL of 0.05 M sodium acetate buffer and incubated with 4 mL of ^{68}GaCl$_3$ at pH 4.0. The reaction mixture was heated for 10 min at 100 °C. Then, ^{68}Ga-DOTA-conjugated peptides were purified using a C18 Sep-Pak Light solid-phase extraction cartridge (Waters Corp., Milford, MA, USA) and eluted in 70% ethanol, and the eluate was dried under air flow and reconstituted in normal saline for injection[58]. The radiochemical purity was determined by HPLC (Shimadzu, Kyoto, Japan). The purified [^{68}Ga]Ga-LyP-1 and [^{68}Ga]Ga-ARA were diluted for PET/CT imaging.

PET/CT imaging

Control (n = 6) or BLM-treated (n = 6) mice were used for the PET/CT study at day 5 or day 18 following BLM administration. Mice were weighed, anesthetized through isoflurane (2%) inhalation and intravenously injected via the tail vein with 5.55–7.4 MBq of [^{68}Ga]Ga-LyP-1 or [^{68}Ga]Ga-ARA. Radioactivity in the syringes was measured using a calibrated gamma counter immediately before and after injection to determine the accurate radioactivity content of the tracer administered to each animal, which was then used for the subsequent calculation of lung radioactivity content in each individual. At 1 h or 2 h post-injection, mice were maintained under anesthesia (1.5% isoflurane) and placed on the scanner bed in a prone position. PET/CT scans were acquired using a TransPET® BioCaliburn® LH scanner (RAYCAN Technology Co., Ltd., Suzhou, China). A PET acquisition (10 min) of a whole-body region was obtained followed by a CT scan of the same region. PET images were reconstructed using the 3-dimensional ordered-subsets expectation maximum (3D-OSEM) algorithm with attenuation correction[59].

Image analysis

For visual interpretation, the fused PET/CT images were obtained using AMIDE software[60]. VOIs corresponding to the lungs were manually drawn with 3D Slicer software (Version 3.10)[61] for CT quantification and to determine their radioactivity content. The lung radioactivity content was expressed in MBq and converted to the SUV. In VOI analysis, mean lung density and SUV$_{mean}$ were measured[45]. Semiautomatic segmentation was also performed using 3D Slicer software (Version 3.10). Semiautomatic segmentation of VOIs on CT scans was based on Hounsfield Unit (HU) thresholds, as described in previous publications[48,62]. Specifically, a range of -800 to -200 HU was used to delineate normal lung regions, corresponding to aerated lung tissue; while -200 to 300 HU was applied to segment non-aerated or fibrotic lung areas. This method employs the “Segment Editor” module in 3D Slicer, which combines manual input with algorithmic tools to refine the segmentation boundaries, thereby enhancing accuracy and efficiency. The segmented regions were validated by comparing the lung CT images of control and BLM-treated animals. This semiautomatic segmentation enabled the quantification of the radioactivity content of [^{68}Ga]Ga-LyP-1 or [^{68}Ga]Ga-ARA in both aerated and non-aerated lung tissues, respectively.

Ex vivo fluorescence imaging of organs

The control or BLM-treated mice were intravenously injected with FITC-LyP-1 or FITC-ARA (200 nmol of peptides per mouse diluted in 150 µL of saline) at day18 following modeling. Mice were anesthetized (0.5% sodium pentobarbital) 2 h later and perfused with PBS via both the left and right ventricles of the heart to remove the blood. The lungs and other organs were imaged with an IVIS Spectrum imaging system with an excitation laser at 488 nm (PerkinElmer, USA). The mean fluorescence intensity of each organ was quantified using Living Image software Version 4.7.3 (PerkinElmer, USA) to reflect the amount of peptide enrichment in the organs. For quantification of the fluorescence intensity of the liver, the gallbladder was removed before imaging to reduce the fluorescence background. After imaging, the lungs were harvested in 10% formalin or in 4% paraformaldehyde for further histological analysis.

Histopathology examinations

Lung samples were fixed in 10% neutral buffered formalin for at least 48 h and processed by routine paraffin embedding. Two 5 µm longitudinal consecutive sections were stained using HE (Beyotime, Shanghai, China) and PSR (Solarbio). The degrees of pulmonary alveolitis and pulmonary fibrosis were observed under an optical microscope according to HE and PSR staining.

Immunofluorescence (IF) analysis

The following antibodies were used for IF staining: rabbit-anti-FITC (Thermo, A889), mouse-anti-FITC (Biolight, TMO0044GeM10-A2F), anti-CD45 (BD Bioscience, 553076), anti-F4/80 (Abcam, ab6640), anti-αSMA (Abcam, ab7817), anti-collagen I (SouthernBiotech, 1310-01), anti-P32 (Abclonal, A1883), Alexa Fluor 555 labeled-phalloidin (Beyotime, China), and Alexa568- or Alexa488-conjugated secondary antibodies (Invitrogen, UK).

Collected lung tissues were fixed with 4% paraformaldehyde for 2 h, dehydrated in 15% sucrose overnight, frozen in OCT (Sakura, Japan), and sliced into 8-µm sections[63]. The sections were penetrated with 0.2% Triton-X 100 PBS for 10 min, blocked with 10% BSA, incubated with primary antibodies overnight at 4 °C, incubated with fluorescently labeled corresponding secondary antibodies, stained with 0.3% Sudan Black (Solarbio) for 5 min, and mounted with DAPI-containing mounting medium.

Costaining of anti-CD45/anti-FITC, anti-F4/80/anti-FITC, and anti-αSMA/anti-FITC, anti-P32/anti-FITC was performed by admixture of primary antibodies. For the co-staining of anti-collagen I/anti-FITC, the DendronFluor TSA multicolor fluorescent labeling kit (Histova biotechnology, Beijing, China) was used according to the manufacturer’s instructions.

A confocal laser scanning microscope (TCS SP8, Leica, Germany) was used to obtain images. The following channels were utilized: Alexa488 (excitation at 488 nm, emission at 525 nm), Alexa568 (excitation at 561 nm, emission at 570 nm), and DAPI (excitation at 405 nm, emission at 450 nm). All excitation light sources were argon ion lasers. A 63 × oil immersion objective lens (NA = 1.4) was employed to ensure high-resolution imaging. Image analysis was performed using ImageJ software (National Institutes of Health, USA).

Statistical analyses

Statistical analyses were performed using GraphPad Prism software version 8 (GraphPad Software Inc., San Diego, USA). Statistical differences were analyzed by unpaired Student’s t test, one-way ANOVA followed by Bonferroni posttest, or Mann–Whitney test. The p values < 0.05 were considered significant. All data are presented as the mean ± SD. Asterisks mark significant differences between different groups (* indicates $p < 0.05$, ** indicates $p < 0.01$, and *** indicates $p < 0.001$). All experiments are representative of at least three independent experiments.

Data availability

The datasets generated during and/or analyzed during the current study are available from the corresponding author on reasonable request.

Received: 27 July 2023; Accepted: 28 October 2024

References

1. Sgalla, G., Kulkarni, T., Antin-Ozerkis, D., Thannickal, V. J. & Richeldi, L. Update in pulmonary fibrosis 2018. *Am. J. Respir. Crit. Care Med.* **200**, 292–300. https://doi.org/10.1164/rccm.201903-0542UP (2019).
2. Wijsenbeek, M., Suzuki, A. & Maher, T. M. Interstitial lung diseases. *Lancet* **400**, 769–786. https://doi.org/10.1016/S0140-6736(22)01052-2 (2022).
3. Rockey, D. C., Bell, P. D. & Hill, J. A. Fibrosis–A common pathway to organ injury and failure. *N. Engl. J. Med.* **372**, 1138–1149. https://doi.org/10.1056/NEJMra1300575 (2015).
4. Meyer, K. C. Pulmonary fibrosis, part I: Epidemiology, pathogenesis, and diagnosis. *Expert Rev. Respir. Med.* **11**, 343–359. https://doi.org/10.1080/17476348.2017.1312346 (2017).
5. Lederer, D. J. & Martinez, F. J. Idiopathic pulmonary fibrosis. *N. Engl. J. Med.* **378**, 1811–1823. https://doi.org/10.1056/NEJMra1705751 (2018).

6. Meyer, K. C. Pulmonary fibrosis, Part II: State-of-the-art patient management. *Expert Rev. Respir. Med.* **11**, 361–376. https://doi.org/10.1080/17476348.2017.1312347 (2017).
7. Wei, Y. et al. Fibroblast-specific inhibition of TGF-beta1 signaling attenuates lung and tumor fibrosis. *J. Clin Invest.* **127**, 3675–3688. https://doi.org/10.1172/JCI94624 (2017).
8. Kekevian, A., Gershwin, M. E. & Chang, C. Diagnosis and classification of idiopathic pulmonary fibrosis. *Autoimmun. Rev.* **13**, 508–512. https://doi.org/10.1016/j.autrev.2014.01.037 (2014).
9. Raghu, G. et al. An official ATS/ERS/JRS/ALAT statement: Idiopathic pulmonary fibrosis: Evidence-based guidelines for diagnosis and management. *Am. J. Respir. Crit. Care Med.* **183**, 788–824. https://doi.org/10.1164/rccm.2009-040GL (2011).
10. Soffer, S. et al. Artificial intelligence for interstitial lung disease analysis on chest computed tomography: A systematic review. *Acad. Radiol.* **29**(Suppl 2), S226–S235. https://doi.org/10.1016/j.acra.2021.05.014 (2022).
11. Loeh, B. et al. Lung CT densitometry in idiopathic pulmonary fibrosis for the prediction of natural course, severity, and mortality. *Chest* **155**, 972–981. https://doi.org/10.1016/j.chest.2019.01.019 (2019).
12. Bybel, B. et al. SPECT/CT imaging: Clinical utility of an emerging technology. *Radiographics* **28**, 1097–1113. https://doi.org/10.1148/rg.284075203 (2008).
13. Schoder, H. & Gonen, M. Screening for cancer with PET and PET/CT: Potential and limitations. *J. Nucl. Med.* **48**(Suppl 1), 4S-18S (2007).
14. Loktev, A. et al. A tumor-imaging method targeting cancer-associated fibroblasts. *J. Nucl. Med.* **59**, 1423–1429. https://doi.org/10.2967/jnumed.118.210435 (2018).
15. Fitzgerald, A. A. & Weiner, L. M. The role of fibroblast activation protein in health and malignancy. *Cancer Metastasis Rev.* **39**, 783–803. https://doi.org/10.1007/s10555-020-09909-3 (2020).
16. Richeldi, L., Collard, H. R. & Jones, M. G. Idiopathic pulmonary fibrosis. *Lancet* **389**, 1941–1952. https://doi.org/10.1016/S0140-6736(17)30866-8 (2017).
17. Schmidkonz, C. Perspective on fibroblast activation protein-specific PET/CT in fibrotic interstitial lung diseases: Imaging fibrosis-A new paradigm for molecular imaging?. *J. Nucl. Med.* **63**, 125–126. https://doi.org/10.2967/jnumed.121.262944 (2022).
18. Xie, N. et al. Glycolytic reprogramming in myofibroblast differentiation and lung fibrosis. *Am. J. Respir. Crit. Care Med.* **192**, 1462–1474. https://doi.org/10.1164/rccm.201504-0780OC (2015).
19. Chen, D. L. et al. [18F]fluorodeoxyglucose positron emission tomography for lung antiinflammatory response evaluation. *Am. J. Respir. Crit. Care Med.* **180**, 533–539. https://doi.org/10.1164/rccm.200904-0501OC (2009).
20. Broens, B. et al. Novel tracers for molecular imaging of interstitial lung disease: A state of the art review. *Autoimmun. Rev.* **21**, 103202. https://doi.org/10.1016/j.autrev.2022.103202 (2022).
21. Laakkonen, P., Porkka, K., Hoffman, J. A. & Ruoslahti, E. A tumor-homing peptide with a targeting specificity related to lymphatic vessels. *Nat. Med.* **8**, 751–755. https://doi.org/10.1038/nm720 (2002).
22. Timur, S. S., Yalcin, G., Cevik, O., Andac, C. & Gursoy, R. N. Molecular dynamics, thermodynamic, and mutational binding studies for tumor-specific LyP-1 in complex with p32. *J. Biomol. Struct. Dyn.* **36**, 1134–1144. https://doi.org/10.1080/07391102.2017.1313779 (2018).
23. Song, N., Zhao, L., Zhu, M. & Zhao, J. Recent progress in LyP-1-based strategies for targeted imaging and therapy. *Drug Deliv.* **26**, 363–375. https://doi.org/10.1080/10717544.2019.1587047 (2019).
24. Abulrob, A. et al. LyP-1 conjugated nanoparticles for magnetic resonance imaging of triple negative breast cancer. *Mol. Imaging Biol.* **20**, 428–435. https://doi.org/10.1007/s11307-017-1140-4 (2018).
25. Sharma, S. et al. Tumor-penetrating nanosystem strongly suppresses breast tumor growth. *Nano Lett.* **17**, 1356–1364. https://doi.org/10.1021/acs.nanolett.6b03815 (2017).
26. Fogal, V., Zhang, L., Krajewski, S. & Ruoslahti, E. Mitochondrial/cell-surface protein p32/gC1qR as a molecular target in tumor cells and tumor stroma. *Cancer Res.* **68**, 7210–7218. https://doi.org/10.1158/0008-5472.CAN-07-6752 (2008).
27. She, Z. G. et al. Plaque-penetrating peptide inhibits development of hypoxic atherosclerotic plaque. *J. Control Release* **238**, 212–220. https://doi.org/10.1016/j.jconrel.2016.07.020 (2016).
28. Hamzah, J. et al. Specific penetration and accumulation of a homing peptide within atherosclerotic plaques of apolipoprotein E-deficient mice. *Proc. Natl. Acad. Sci. U. S. A.* **108**, 7154–7159. https://doi.org/10.1073/pnas.1104540108 (2011).
29. Teesalu, T., Sugahara, K. N., Kotamraju, V. R. & Ruoslahti, E. C-end rule peptides mediate neuropilin-1-dependent cell, vascular, and tissue penetration. *Proc. Natl. Acad. Sci. U. S. A.* **106**, 16157–16162. https://doi.org/10.1073/pnas.0908201106 (2009).
30. Ogawa, T., Shichino, S., Ueha, S. & Matsushima, K. Macrophages in lung fibrosis. *Int. Immunol.* **33**, 665–671. https://doi.org/10.1093/intimm/dxab040 (2021).
31. Aono, Y. et al. Imatinib as a novel antifibrotic agent in bleomycin-induced pulmonary fibrosis in mice. *Am. J. Respir. Crit. Care Med.* **171**, 1279–1285. https://doi.org/10.1164/rccm.200404-531OC (2005).
32. Izbicki, G., Segel, M. J., Christensen, T. G., Conner, M. W. & Breuer, R. Time course of bleomycin-induced lung fibrosis. *Int. J. Exp. Pathol.* **83**, 111–119. https://doi.org/10.1046/j.1365-2613.2002.00220.x (2002).
33. Della Latta, V., Cecchettini, A., Del Ry, S. & Morales, M. A. Bleomycin in the setting of lung fibrosis induction: From biological mechanisms to counteractions. *Pharmacol. Res.* **97**, 122–130. https://doi.org/10.1016/j.phrs.2015.04.012 (2015).
34. Desogere, P. et al. Type I collagen-targeted PET probe for pulmonary fibrosis detection and staging in preclinical models. *Sci. Transl. Med.* https://doi.org/10.1126/scitranslmed.aaf4696 (2017).
35. Wynn, T. A. Cellular and molecular mechanisms of fibrosis. *J. Pathol.* **214**, 199–210. https://doi.org/10.1002/path.2277 (2008).
36. Principi, L. et al. Proteomic fingerprint of lung fibrosis progression and response to therapy in bleomycin-induced mouse model. *Int. J. Mol. Sci.* https://doi.org/10.3390/ijms24054410 (2023).
37. Decaris, M. L. et al. Proteomic analysis of altered extracellular matrix turnover in bleomycin-induced pulmonary fibrosis. *Mol. Cell Proteomics* **13**, 1741–1752. https://doi.org/10.1074/mcp.M113.037267 (2014).
38. Weatherley, N. D. et al. Experimental and quantitative imaging techniques in interstitial lung disease. *Thorax* **74**, 611–619. https://doi.org/10.1136/thoraxjnl-2018-211779 (2019).
39. Song, S. et al. Intracellular hydroxyproline imprinting following resolution of bleomycin-induced pulmonary fibrosis. *Eur. Respir. J.* https://doi.org/10.1183/13993003.00864-2021 (2022).
40. Katzen, J. & Beers, M. F. Contributions of alveolar epithelial cell quality control to pulmonary fibrosis. *J. Clin. Invest.* **130**, 5088–5099. https://doi.org/10.1172/JCI139519 (2020).
41. Gu, Y., Lawrence, T., Mohamed, R., Liang, Y. & Yahaya, B. H. The emerging roles of interstitial macrophages in pulmonary fibrosis: A perspective from scRNA-seq analyses. *Front. Immunol.* **13**, 923235. https://doi.org/10.3389/fimmu.2022.923235 (2022).
42. Geng, Y. et al. PEAR1 regulates expansion of activated fibroblasts and deposition of extracellular matrix in pulmonary fibrosis. *Nat. Commun.* **13**, 7114. https://doi.org/10.1038/s41467-022-34870-w (2022).
43. Montesi, S. B., Desogere, P., Fuchs, B. C. & Caravan, P. Molecular imaging of fibrosis: Recent advances and future directions. *J. Clin. Invest.* **129**, 24–33. https://doi.org/10.1172/JCI122132 (2019).
44. Baues, M. et al. Fibrosis imaging: Current concepts and future directions. *Adv. Drug Deliv. Rev.* **121**, 9–26. https://doi.org/10.1016/j.addr.2017.10.013 (2017).
45. Fraioli, F. et al. Synergistic application of pulmonary (18)F-FDG PET/HRCT and computer-based CT analysis with conventional severity measures to refine current risk stratification in idiopathic pulmonary fibrosis (IPF). *Eur. J. Nucl. Med. Mol. Imaging* **46**, 2023–2031. https://doi.org/10.1007/s00259-019-04386-5 (2019).

46. Yoon, H. Y., Lee, S. H., Ha, S., Ryu, J. S. & Song, J. W. The value of (18)F-FDG PET/CT in evaluating disease severity and prognosis in idiopathic pulmonary fibrosis patients. *J. Korean Med. Sci.* **36**, e257. https://doi.org/10.3346/jkms.2021.36.e257 (2021).
47. Yoon, H. Y., Lee, S. H., Ha, S., Ryu, J. S. & Song, J. W. (18)F-FDG PET/CT predicts acute exacerbation in idiopathic pulmonary fibrosis after thoracic surgery. *BMC Pulm. Med.* **21**, 294. https://doi.org/10.1186/s12890-021-01659-4 (2021).
48. Rosenkrans, Z. T. et al. [(68) Ga]Ga-FAPI-46 PET for non-invasive detection of pulmonary fibrosis disease activity. *Eur. J. Nucl. Med. Mol. Imaging* **49**, 3705–3716. https://doi.org/10.1007/s00259-022-05814-9 (2022).
49. Rohrich, M. et al. Fibroblast activation protein-specific PET/ct imaging in fibrotic interstitial lung diseases and lung cancer: A translational exploratory study. *J. Nucl. Med.* **63**, 127–133. https://doi.org/10.2967/jnumed.121.261925 (2022).
50. Lindner, T. et al. (18)F-labeled tracers targeting fibroblast activation protein. *EJNMMI Radiopharm. Chem.* **6**, 26. https://doi.org/10.1186/s41181-021-00144-x (2021).
51. She, Z. G., Liu, X., Kotamraju, V. R. & Ruoslahti, E. Clot-targeted micellar formulation improves anticoagulation efficacy of bivalirudin. *ACS Nano* **8**, 10139–10149. https://doi.org/10.1021/nn502947b (2014).
52. Seo, J. W. et al. (64)Cu-labeled LyP-1-dendrimer for PET-CT imaging of atherosclerotic plaque. *Bioconjug. Chem.* **25**, 231–239. https://doi.org/10.1021/bc400347s (2014).
53. Yu, X. et al. Ultrasmall semimetal nanoparticles of bismuth for dual-modal computed tomography/photoacoustic imaging and synergistic thermoradiotherapy. *ACS Nano* **11**, 3990–4001. https://doi.org/10.1021/acsnano.7b00476 (2017).
54. Jiang, Y. et al. Magnetic mesoporous nanospheres anchored with LyP-1 as an efficient pancreatic cancer probe. *Biomaterials* **115**, 9–18. https://doi.org/10.1016/j.biomaterials.2016.11.006 (2017).
55. Song, N. et al. LyP-1-modified multifunctional dendrimers for targeted antitumor and antimetastasis therapy. *ACS Appl. Mater. Interfaces* **12**, 12395–12406. https://doi.org/10.1021/acsami.9b18881 (2020).
56. Fang, Y. H. & Muzic, R. F. Jr. Spillover and partial-volume correction for image-derived input functions for small-animal 18F-FDG PET studies. *J. Nucl. Med.* **49**, 606–614. https://doi.org/10.2967/jnumed.107.047613 (2008).
57. Cuplov, V. et al. Issues in quantification of registered respiratory gated PET/CT in the lung. *Phys. Med. Biol.* **63**, 015007. https://doi.org/10.1088/1361-6560/aa950b (2017).
58. Viitanen, R. et al. First-in-humans study of (68)Ga-DOTA-Siglec-9, a PET ligand targeting vascular adhesion protein 1. *J. Nucl. Med.* **62**, 577–583. https://doi.org/10.2967/jnumed.120.250696 (2021).
59. Yao, R. et al. Performance characteristics of the 3-D OSEM algorithm in the reconstruction of small animal PET images. Ordered-subsets expectation-maximixation. *IEEE Trans. Med. Imaging* **19**, 798–804. https://doi.org/10.1109/42.876305 (2000).
60. Loening, A. M. & Gambhir, S. S. AMIDE: A free software tool for multimodality medical image analysis. *Mol. Imaging* **2**, 131–137. https://doi.org/10.1162/15353500200303133 (2003).
61. Fedorov, A. et al. 3D slicer as an image computing platform for the quantitative imaging network. *Magn. Reson. Imaging* **30**, 1323–1341. https://doi.org/10.1016/j.mri.2012.05.001 (2012).
62. Tanguy, J. et al. [(18)F]FMISO PET/CT imaging of hypoxia as a non-invasive biomarker of disease progression and therapy efficacy in a preclinical model of pulmonary fibrosis: Comparison with the [(18)F]FDG PET/CT approach. *Eur. J. Nucl. Med. Mol. Imaging* **48**, 3058–3074. https://doi.org/10.1007/s00259-021-05209-2 (2021).
63. Mann, A. P. et al. A peptide for targeted, systemic delivery of imaging and therapeutic compounds into acute brain injuries. *Nat. Commun.* **7**, 11980. https://doi.org/10.1038/ncomms11980 (2016).

Acknowledgements

This work was supported by grants from National Science Foundation, China (81970364, 82271777, 82270390 and 81970070), research fund from medical Sci-Tech innovation platform of Zhongnan Hospital, Wuhan University (Project. PTXM2023009), the Hubei Province Innovation Platform Construction Project (20204201117303072238), the Henan Charity General Federation (GDXZ2023016). We thank Shaoping Liu at the Medical Science Research Center of Zhongnan hospital for the technical support, and Hao Wang, Dawei Jiang at the Wuhan Union Hospital for offering Ga-68 ions and helpful discussion. We also thank Hubei Provincial Engineering Research Center of Model Animal for their support of animal models.

Author contributions

All authors contributed to the study conception and design. Animal experiments were performed by Y.H., Z.C. and S.T. Immunopathological and cell biology experiments were performed by M.Y., T.P., R.S., Z.Y., Z.T. and F.H. PET/CT imaging was performed by R.S., T.P., J.L., J.J., L.W., and image analysis was performed by J.L. and J.J. The writing of first draft was performed by J.L., M.Y., T.P. and E.Z. The manuscript was revised by R.S., X.-J.Z., Z.-G.S., H.L. and E.Z. All authors commented on previous versions of the manuscript. All authors read and approved the final manuscript. J.L., R.S. and T.P. contribute equally to this article. E.Z., X.-J.Z. and H.L. are co-corresponding authors.

Declarations

Competing interests

The authors have no relevant financial or non-financial interests to disclose.

Additional information

Supplementary Information The online version contains supplementary material available at https://doi.org/10.1038/s41598-024-78068-0.

Correspondence and requests for materials should be addressed to H.L., X.-J.Z. or E.Z.

Reprints and permissions information is available at www.nature.com/reprints.